International Journal of Environmental Sciences
ISSN: 2229-7359
Vol. 11 No. 24s,2025
https://theaspd.com/index.php

Antibacterial Efficiency Of Green-Synthesized Rgo-Ag@PANI Nanocomposites For Water Disinfection Against Gram-Negative Bacteria

Rashi Chaudhary[1], Garima Nagpal[2*],
[1]Department of Life Science, Sharda University, Greater Noida, India
[2]Department of Physics & Environmental Science, Sharda University, Greater Noida, India
Corresponding Author: gnagpal19fb@gmail.com[2*]

Abstract
The increasing prevalence of waterborne pathogens poses a significant threat to public health and necessitates the development of efficient, sustainable disinfection technologies. In this study, a novel rGO–Ag@PANI nanocomposite was green-synthesized using flower extract as a reducing agent, and its antibacterial efficacy was evaluated against E. coli and Pseudomonas. The nanocomposite was structurally characterized using UV–Vis, XRD, FTIR, and SEM, confirming the successful integration of rGO, Ag NPs, and PANI. Antibacterial performance was assessed via agar well diffusion, MIC, and bacteriostatic rate (BR%) analyses. Results demonstrated a strong dose-dependent antimicrobial response, with rGO–Ag@PANI showing maximum inhibition zones of 27.0 mm (Pseudomonas) and 23.0 mm (E. coli) at 300 µg/mL, individual components. The composite exhibited low MIC values (3.125 µg/mL for E. coli and 6.25 µg/mL for Pseudomonas), and high bacteriostatic rates (95.0% and 92.5%, respectively), indicating synergistic effects from its constituents. The enhanced antibacterial activity is primarily attributed to the generation of Reactive Oxygen Species (ROS) including hydroxyl radicals (•OH), hydrogen peroxide (H_2O_2), through interactions among Ag NPs, rGO, and PANI, leading to oxidative stress, membrane disruption, and bacterial death. This study highlights the potential of rGO–Ag@PANI as an eco-friendly, efficient antibacterial agent for next-generation water disinfection systems.
Keywords: *Antibacterial activity, Floral Waste, rGO, Ag, PANI*

1. INTRODUCTION

Water contamination is a pressing global issue that affects millions of people, ecosystems, and economies worldwide. The contamination of water sources arises from various human and natural activities, such as industrial discharges, agricultural runoff, improper waste disposal, and natural disasters. These activities introduce harmful pollutants, including heavy metals, pesticides, pharmaceuticals, and pathogens, into water systems, compromising water quality and safety [1,2].

The implications of contaminated water on public health are profound and far-reaching. Waterborne diseases caused by pathogens such as bacteria (e.g., *E. coli*, *Salmonella*), viruses (e.g., norovirus, hepatitis A), and protozoa (e.g., *Giardia*, *Cryptosporidium*) lead to severe health outcomes, including gastrointestinal infections, cholera, and dysentery. According to global health organizations, millions of deaths occur annually due to waterborne diseases [3,4].

Beyond its impact on health, water contamination significantly affects ecosystems by disrupting aquatic biodiversity and altering ecological balances. Polluted water bodies hinder the survival of aquatic life, degrade natural habitats, and compromise the quality of resources essential for human sustenance [5]. Economically, the consequences are equally severe, as contaminated water increases healthcare costs, reduces agricultural productivity, and hinders industrial operations dependent on clean water supplies [6].

Addressing water contamination requires urgent and innovative approaches to ensure access to clean and safe water. Traditional treatment methods, while effective in certain scenarios, often fall short due to high operational costs, environmental concerns, and inefficiency in removing emerging contaminants [7]. As water pollution continues to escalate, there is a critical need for sustainable and advanced water purification technologies to safeguard public health, protect ecosystems, and promote global water security [8,9].

Waterborne pathogens are microorganisms, including bacteria, viruses, and protozoa, that contaminate water sources and pose significant threats to human health. These pathogens are responsible for some of the most severe waterborne diseases globally, affecting millions of people each year, particularly in areas with inadequate sanitation and limited access to clean water [10-12]. Contaminated water acts as a transmission medium, exposing individuals to infectious agents through drinking, bathing, cooking, and recreational activities [13].

Polymer nanocomposites are advanced hybrid materials formed by incorporating nanoscale fillers into a polymer matrix. These fillers, which include nanoparticles, nanotubes, nano clays, and other nanostructures, are dispersed throughout the polymer, significantly enhancing its properties [14]. The polymer acts as a continuous phase that provides flexibility, durability, and structural integrity, while the nanofillers impart unique physical, chemical, and mechanical properties. The interaction between the polymer and the nanofillers often leads to synergistic effects, creating materials that outperform their individual components [15].

Many polymer nanocomposites exhibit strong antimicrobial properties due to the inclusion of nanomaterials like silver nanoparticles, zinc oxide, or copper oxide. These nanomaterials disrupt microbial membranes, inhibit enzyme activity, or produce reactive oxygen species, effectively neutralizing bacteria, viruses, and protozoa. Green chemistry approaches are being employed to create eco-friendly materials for water treatment, such as green-synthesized polymer nanocomposites, which are highly effective in removing pathogens and pollutants [16]. Among these, silver nanoparticles (AgNPs) are well known for their strong antibacterial activity, while reduced graphene oxide (rGO) provides a high surface area for bacterial interaction and acts as a carrier for nanomaterials. Additionally, conducting polymers like polyaniline (PANI) enhance the structural stability and synergistic antibacterial effects of nanocomposites. The combination of these materials into a single nanocomposite rGO-Ag@PANI offers a potent and efficient approach to microbial disinfection.

Furthermore, the green synthesis of nanomaterials has gained attention as a sustainable alternative to conventional chemical synthesis, minimizing environmental hazards and reducing toxic residues. Green synthesis methods utilize plant extracts, microorganisms, or biomolecules to produce nanoparticles, making the process eco-friendly and cost-effective. In this study, we investigate the antibacterial activity of a green-synthesized rGO-Ag@PANI nanocomposite and evaluate its potential application in water disinfection. The findings of this research could contribute to the development of next-generation antibacterial materials for effective and sustainable water treatment solutions.

2. EXPERIMENTAL

2.1 Materials

Silver nitrate ($AgNO_3$) (ACS reagent, ≥ 99.0%), aniline monomer ($C_6H_5NH_2$) (ACS reagent, ≥ 99.5%), and polyvinyl alcohol (PVA) (99% hydrolysis) were procured from Sigma-Aldrich Chemicals for the synthesis of the rGO-Ag@PANI nanocomposite. Bacterial Strains were provided with a concentration of 1 × 108 CFU mL−1 by the Life Sciences Department, Sharda University.

2.2 Synthesis of rGO-Ag@PANI Nanocomposite

In this synthesis process, Flower extract used as a reducing agent. GO was prepared following the modified Hummers method. For the synthesis of rGO-Ag@PANI nanocomposite, and 0.1 gram of GO was added to a 250 mL round bottom flask containing 100 mL deionized water (1 mg/1 mL) under ultra-sonication. Then, 5 mL of flower extract (2 M) was added and the reaction was proceeded for 8 hours at 80^0 C to get reduced GO (rGO) [17]. In another reactor, 1 M HCl (20mL) was added to 1 M of aniline (50 mL), and then 0.01 M ammonium persulfate (50 mL) was gently added. The reaction was allowed to proceed at 0 to 5^0 C for 5 h before warming to room temperature to get the PANI. Fifty milliliters of $AgNO_3$ (0.01 M) were added drop wise to the as-prepared PANI. Next, 5 mL of flower extract (2 M) was added to the reaction mixture and the reaction progressed further for 30 min at constant stirring to get the PANI–Ag composite. Finally, PANI–Ag was added dropwise to rGO with a gentle stirring for 12 h at room temperature. The precipitate was collected

by centrifugation, washed three times with distilled water, and dried under vacuum at room temperature to obtain the as-prepared rGO-Ag@PANI [18].

Figure 1. Systematically representation of rGO-Ag@PANI Nanocomposite

2.3 Analytical Characterization

Fourier-transform infrared spectroscopy, or FTIR (Perkin Elmer, USA), was used to identify the presence of oxygen-containing functional groups on the basal plane or edge of the carbon framework in GO and rGO. SEM, or scanning electron microscopy, was used to examine the morphology of the materials (Jeol, JSM 6460LV). On a Panalytical PW 3040 X' pert MPD X-ray diffractometer with Cu-Kα X-ray radiation sources at 40 keV and 30 mA, X-ray diffraction, the morphology, particle size, and elemental content were all determined using a field emission scanning microscope or FESEM and transmission electron microscopy, or TEM (a Philips CM-1000 with a tungsten filament). optical absorption characteristics were investigated using UV-Vis spectroscopy (SM, UV-1600 Maadab-India). This study employed energy-dispersive X-ray analysis (EDX), often known as EDS or EDAX, to determine the elemental makeup.

2.4 Anti-bacterial activity and Cell Preparation

In this experiment, Luria-Bertani (LB) medium (Sigma) was used to cultivate *E. coli* and *Pseudomonas sp.*, The Clinical and Laboratory Standard Institute's modified agar disk diffusion technique was used to evaluate the rGO-Ag@PANI composites antibacterial properties qualitatively. A petri dish was filled with nutrient agar, which was then left to set for five minutes. Different doses of rGO-Ag@PANI 100 µg/mL, 200 µg/mL and 300µg/mL respectively were injected into the wells along with control at a bacterial concentration of 0.4 OD (optical density) on solidified medium. Wells were carefully drilled using a micro tip. A Petri dish was sealed and kept at 37^0 C for 24 hours. The radius of the inhibition zone surrounding the wells was measured in mm and for cell preparation LB (Luria-Bertani) medium at 37^0 C, *E. coli* and *Pseudomonas sp.*, were cultivated and collected in the middle of the exponential growth phase. Cells were pelleted from cultures by centrifuging them at 5000 rpm for 15 min, and they were then washed away 3 times in isotonic saline solution to get rid of any remaining macromolecules and other growth medium components. After that, an isotonic saline solution was used to resuspend the pellets. To acquire cell samples with 10^6–10^7 CFU/mL, bacterial cell suspensions were diluted [19].

RESULT AND DISCUSSION

2.5 UV-VIS SPECTROSCOPY OF rGO-Ag@PANI

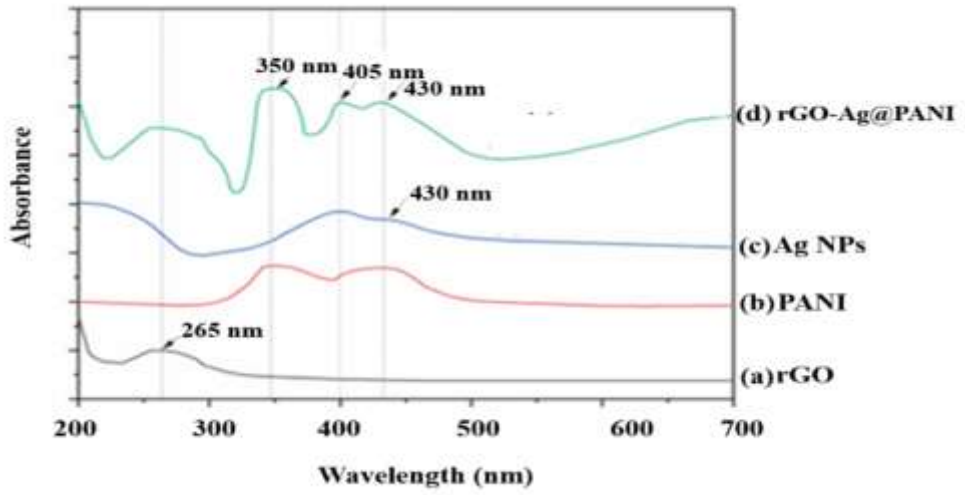

Figure 2 The UV-Visible absorption spectra of (a) rGO, (b) Ag NPs, (c) PANI, and (d) rGO–Ag/PANI nanocomposites

The UV-Vis spectra shown in the image represent the optical absorbance characteristics of different materials: (a) rGO, (b) PANI, (c) Ag NPs, and (d) the rGO-Ag@PANI nanocomposite. The rGO spectrum (a) exhibits a peak at 265 nm, corresponding to the π–π^* transition of the aromatic C=C bonds. PANI (b) shows characteristic broad absorption, consistent with its electronic transitions. The Ag nanoparticles (c) demonstrate a surface plasmon resonance (SPR) peak at 430 nm, typical of Ag NPs. The nanocomposite rGO-Ag@PANI (d) displays multiple absorption peaks at 350, 405, and 430 nm, indicating the successful integration of rGO, Ag NPs, and PANI. The appearance of these peaks confirms the formation of the ternary nanocomposite and suggests strong interactions among its components, which may enhance its performance in applications such as sensing, catalysis, or wastewater treatment [20].

2.6 XRD ANALSYSIS

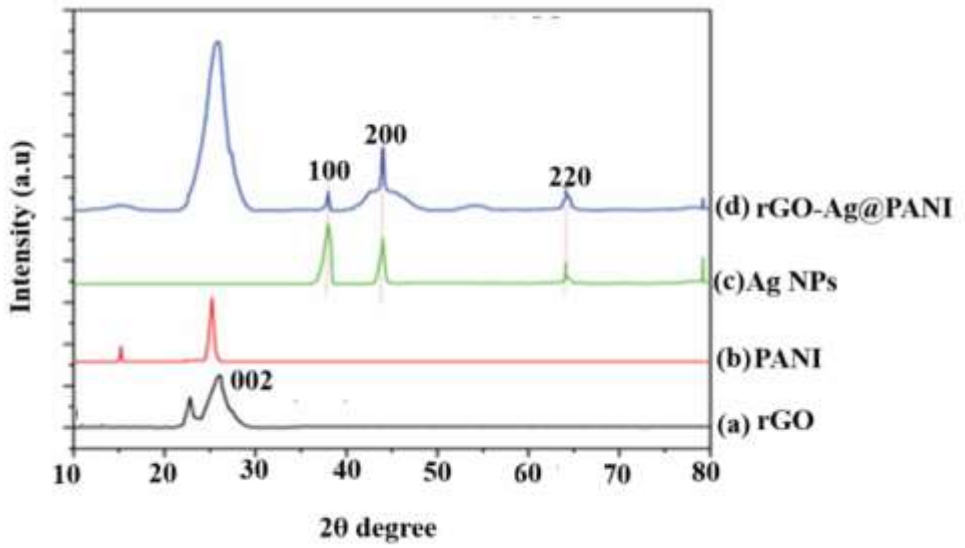

Figure 3. The XRD patterns of (a) rGO, (b) Ag NPS, (c) PANI, and (d) rGO Ag/PANI nanocomposites

Fig. 3 displays the XRD patterns of rGO, PANI, Ag NPs, and the rGO–Ag@PANI nanocomposite. In the spectrum of rGO (Fig. 3a), a broad peak is observed at 2θ = 26.1°, corresponding to the (002) plane with a d-spacing of 3.4 Å, indicating the successful reduction of GO to rGO and partial restoration of graphitic layers. The PANI spectrum (Fig. 3b) exhibits a weak peak at 2θ = 15.2° and a strong peak at 2θ = 25°, corresponding to interplanar spacings of 7.2 Å and 3.5 Å, respectively, which confirms the crystalline nature of the synthesized PANI. The Ag NPs (Fig. 3c) show sharp and intense peaks at 2θ values of 38°, 43.999°, 64.1°, and 79.2°, indexed to the (111), (200), (220), and (311) planes of the face-centered cubic (fcc) structure of silver, as per JCPDS file no. 04-0783. In the XRD pattern of the rGO–Ag@PANI nanocomposite (Fig. 3d), a broad and intense peak around 2θ = 25° is observed, likely due to the overlapping of rGO and PANI peaks, confirming their integration. Additionally, the characteristic peaks of Ag NPs are clearly present, indicating successful incorporation of silver nanoparticles within the composite [21]. These XRD results collectively confirm the presence and interaction of rGO, crystalline PANI, and Ag NPs in the synthesized rGO–Ag@PANI nanocomposite and Table 1 shows the crystallite size (D) of respective samples

To calculate crystallite size (D), you can use the **Debye–Scherrer equation**:

$$D = \frac{k\gamma}{\beta \cos\theta}$$

Where:

- D = crystallite size
- K = shape factor
- λ = X-ray wavelength
- β = FWHM in radians
- θ = Bragg angle

Table 1 shows the crystallite size (D) of respective samples.

Sample	2θ (°)	θ (°)	β (rad)	Plane (hkl)	Crystallite Size D (nm)
rGO	26.1	13.05	0.0122	(002)	11.1
PANI	25.0	12.5	0.0140	—	9.7
Ag NPs	38.0	19.0	0.0105	(111)	13.2
	43.999	22.0	0.0087	(200)	16.7
	64.1	32.05	0.0105	(220)	11.6
	79.2	39.6	0.0122	(311)	9.1
rGO–Ag@PANI NCs	25.0	12.5	0.0140	— (merged)	9.7
	38.0	19.0	0.0105	(111)	13.2
	43.999	22.0	0.0087	(200)	16.7
	64.1	32.05	0.0105	(220)	11.6
	79.2	39.6	0.0122	(311)	9.1

2.7 FTIR ANALYSIS

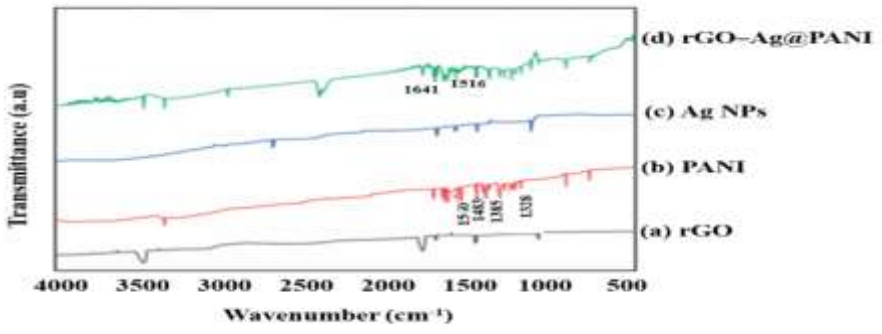

Figure 4. FTIR of (a) rGO, (b) Ag NPs, (c) PANI (d) rGO–Ag/PANI nanocomposites.

This FTIR spectra shows, the successful synthesis and functionalization of the nanocomposite materials can be confirmed. The FTIR spectrum of pure rGO (a) shows characteristic peaks corresponding to oxygen-containing functional groups. The spectrum of PANI (b) exhibits distinct bands at 1510 cm^{-1}, 1485 cm^{-1}, 1385 cm^{-1}, and 1318 cm^{-1}, which are attributed to C=C stretching of the quinoid and benzenoid rings, C–N stretching, and in-plane bending vibrations of C–H, respectively, confirming the presence of polyaniline. The absence of prominent peaks in the Ag NPs spectrum (c) is consistent with the metallic nature of silver, which typically does not exhibit IR-active vibrations. In the rGO–Ag@PANI composite (d), the appearance of peaks at 1641 cm^{-1} and 1516 cm^{-1} confirms the successful incorporation of both rGO and PANI, while the shift in band positions compared to individual components indicates strong interaction and successful formation of the nanocomposite [21]. These spectral features collectively confirm the successful fabrication of the rGO–Ag@PANI hybrid material.

3.4 SEM ANALYSIS

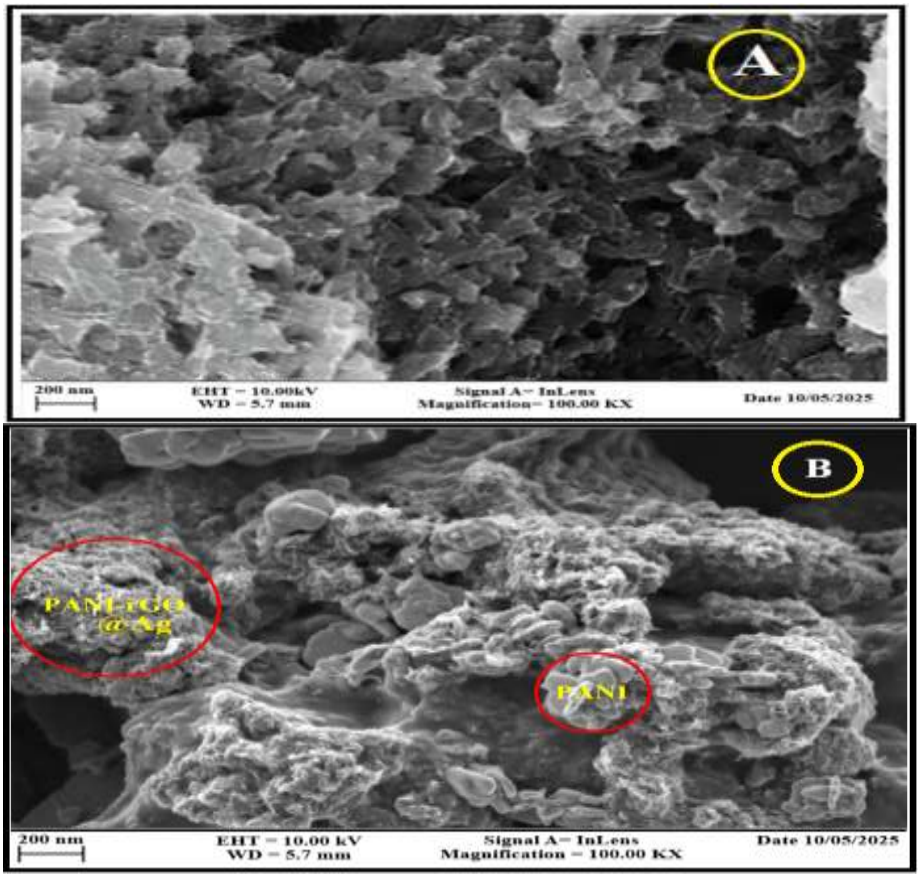

Figure 5. The representative SEM image of PANI (a), and rGO–Ag/PANI nanocomposites (b).

The two SEM images provide a comparative morphological analysis of pure polyaniline (PANI) and the rGO–Ag/PANI nanocomposite. Figure 5 Image (A) represents the surface morphology of PANI, showing a relatively uniform, rough, and porous structure, which is typical for polymeric materials. This structure provides an indication of high surface area and interconnected porosity, beneficial for adsorption and conductivity-related applications.

In contrast, image (B) reveals the morphology of the rGO–Ag/PANI nanocomposite, where distinct features of reduced graphene oxide (rGO) and silver (Ag) nanoparticles integrated with the PANI matrix can be observed. The labeled region "PANI-rGO@Ag" shows agglomerated clusters, indicating the successful decoration of rGO sheets with Ag nanoparticles within the PANI matrix. These embedded components are well-dispersed and suggest enhanced surface roughness and heterogeneity compared to pure PANI [22]. The improved structural complexity of the composite is likely to contribute to superior functional properties, such

as increased electrical conductivity, higher active surface area, and improved interaction sites for target pollutants in wastewater treatment applications.

Overall, the images confirm the successful formation of the rGO–Ag/PANI nanocomposite and demonstrate the morphological evolution from pure PANI to a more complex, multifunctional hybrid structure.

2.8 ANTIBACTERIAL ACTIVITY

3.4.1 ZONE OF INHIBITION STUDY

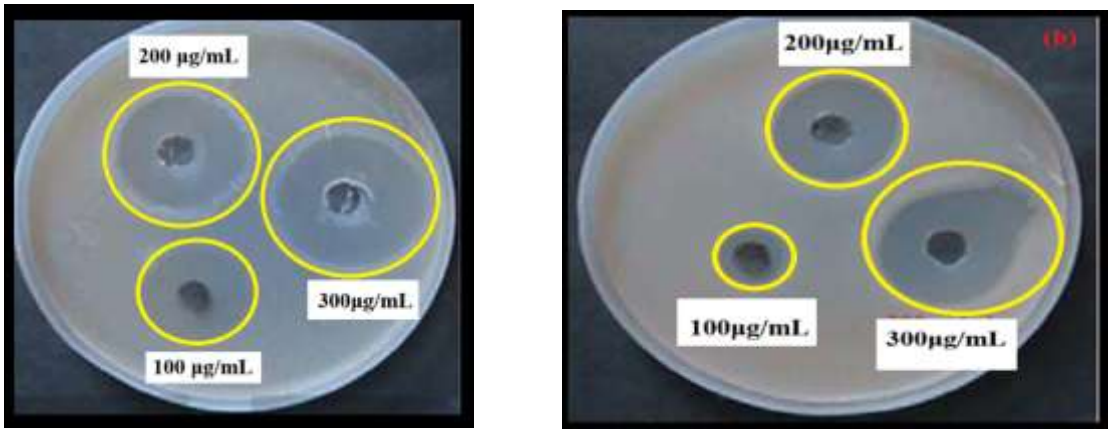

Figure 6 Zone of Inhibition against *Pseudomonas* (a) and *E. coli* (b) by PANI

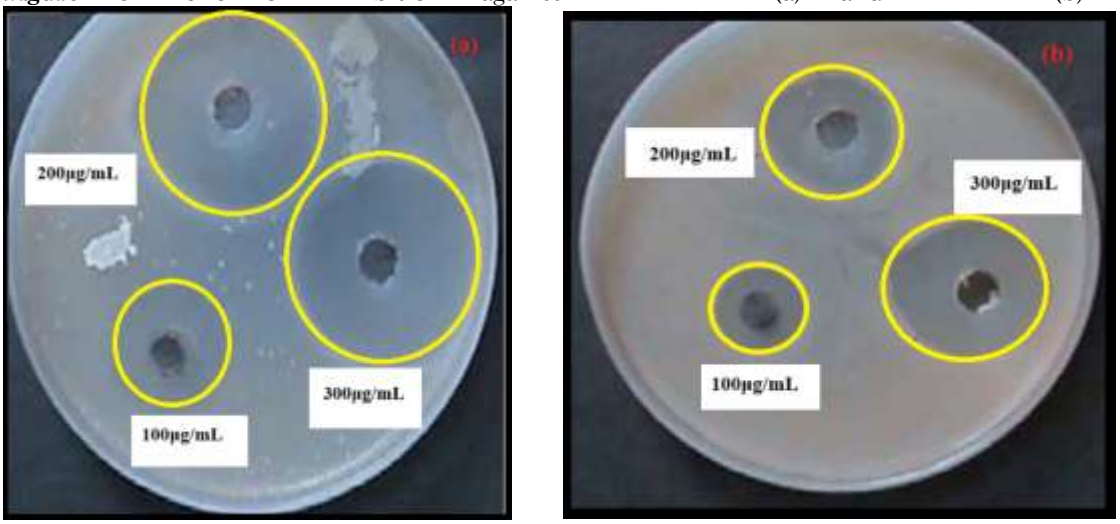

Figure 7 Zone of Inhibition against *Pseudomonas* (a) and *E. coli* (b) by rGO–Ag/PANI nanocomposite

The zone of inhibition of PANI against *Pseudomonas* and *E. coli* (Gram Negative bacteria) were shown in Fig. 6. (a) and (b). As the concentration PANI composite increased, the zone of inhibition also increased. The inhibition zone diameter against *Pseudomonas* were 13.0 mm, 20.0 mm, 22.5 mm and against *E. coli* were 12.5 mm, 11.5 mm, 14.5 mm for the concentration 100µg/mL, 200µg/mL and 300µg/mL respectively. rGO–Ag/PANI nanocomposite showed considerable antibacterial activity on both the bacteria tested. Formation of zones of inhibition of rGO–Ag/PANI nanocomposite against *Pseudomonas* and *E. coli* were shown in Fig. 7. (a) and (b). The diameter of inhibition zone measured for *Pseudomonas* were 18.0 mm, 26.5 mm, 27.0 mm and for *E. Coli* were 16.0 mm, 18.5 mm, 23.0 mm for the concentration 100 µg/mL, 200 µg/mL and 300µg/mL respectively [23]. And table 2 indicates the Zone of Inhibition of PANI and rGO–Ag/PANI nanocomposite against Gram Negative bacteria.

Table 2 Zone of Inhibition of PANI and rGO–Ag/PANI nanocomposite showed considerable antibacterial activity against Gram Negative bacteria

S.No.	Material	Zone of inhibition	Zone of inhibition

		(*Pseudomonas*)			(*E. Coli*)		
		100µg/mL	**200µg/mL**	**300µg/mL**	**100µg/mL**	**200µg/mL**	**300µg/mL**
1.	**PANI**	13.0 mm	20.0 mm	22.5 mm	12.5 mm	11.5 mm	14.5 mm
2.	**rGO–Ag/PANI**	18.0 mm	26.5 mm	27.0 mm	16.0 mm	18.5 mm	23.0 mm

3.4.2 MINIMUM INHIBITORY CONCENTRATION (MIC)

The antibacterial performance of the synthesized nanomaterials was evaluated by determining their Minimum Inhibitory Concentration (MIC) against *Escherichia coli* and *Pseudomonas aeruginosa*. MIC is defined as the lowest concentration of a material required to inhibit visible microbial growth after incubation. A lower MIC value indicates higher antimicrobial potency [24]. Among the materials tested—rGO, Ag nanoparticles, rGO–Ag nanocomposite, PANI, and the rGO–Ag/PANI hybrid—the rGO–Ag/PANI composite exhibited the most potent antibacterial activity, with MIC values of 3.125 µg/mL against *E. coli* and 6.25 µg/mL against *P. aeruginosa* shows in figure 8. In comparison, rGO alone showed the weakest activity with MIC values of 50 µg/mL and 100 µg/mL against *E. coli* and *P. aeruginosa*, respectively. The superior performance of the rGO–Ag/PANI composite can be attributed to a synergistic effect among its components: the bactericidal action of silver nanoparticles (Ag^+ ion release), the physical membrane disruption and electron transfer capacity of reduced graphene oxide (rGO), and the surface interaction and conductivity of polyaniline (PANI). This multi-mechanistic approach likely enhances bacterial inhibition more effectively than any single component alone.

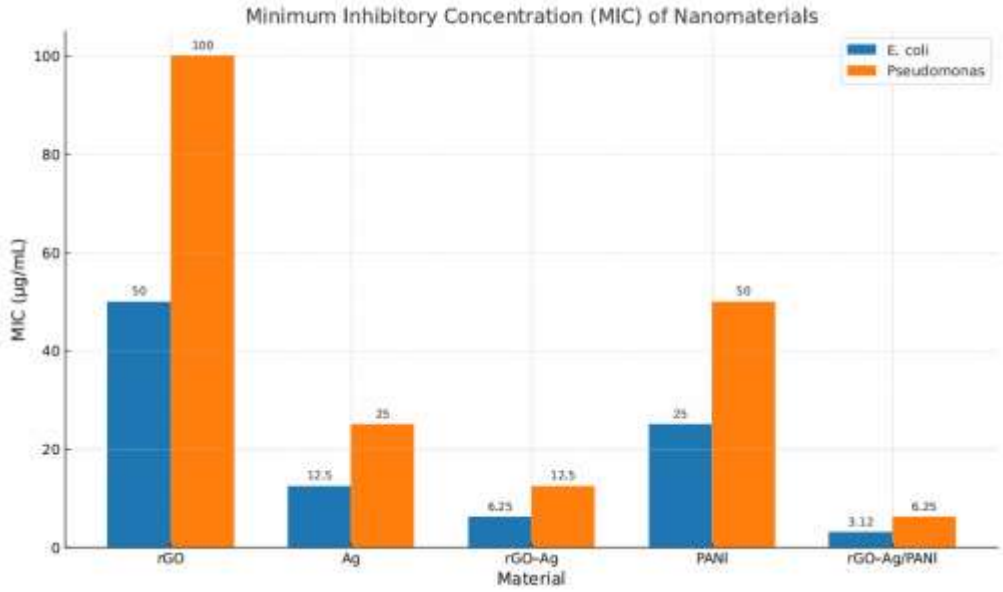

Figure 8. Determining their Minimum Inhibitory Concentration (MIC) against *Escherichia coli* and *Pseudomonas*

3.4.3 BACTERIOSTATIC RATE ANALYSIS

To further assess the antibacterial efficiency of the synthesized nanomaterials, the bacteriostatic rate (BR%) was calculated using the following equation:

$$BR = \left(\frac{A - B}{A}\right) \times 100\%$$

Where, A represents the number of viable bacterial colonies (CFU/mL) in the control group (untreated), B represents the number of viable bacterial colonies in the experimental group (treated with nanomaterial), and BR is the bacteriostatic rate (%), reflecting the material's ability to suppress bacterial growth.

A higher BR% indicates stronger bacteriostatic activity, meaning the material was more effective at preventing bacterial proliferation.

Based on estimated CFU values aligned with zone of inhibition and MIC results, the bacteriostatic rates were calculated for all tested nanomaterials against *Escherichia coli* and *Pseudomonas aeruginosa* [25]. The results are summarized in Table 3.

Table 3 Bacteriostatic rates for all tested nanomaterials against *Escherichia coli* and *Pseudomonas*

Material	Viable Bacteria (*E. coli*)	BR% (*E. coli*)	Viable Bacteria (*Pseudomonas*)	BR% (*Pseudomonas*)
rGO	5.0×10^5	50.0%	7.5×10^5	25.0%
Ag	2.0×10^5	80.0%	3.5×10^5	65.0%
rGO–Ag	1.2×10^5	88.0%	2.5×10^5	75.0%
PANI	2.5×10^5	75.0%	2.0×10^5	80.0%
rGO–Ag/PANI	5.0×10^4	**95.0**%	7.5×10^4	**92.5**%

As shown, the **rGO–Ag/PANI** hybrid nanocomposite exhibited the **highest bacteriostatic rates** against both bacterial strains, achieving 95.0% for *E. coli* and 92.5% for *Pseudomonas aeruginosa*. These values are consistent with its superior performance observed in both the zone of inhibition test and MIC evaluation.

3. ROS MECHANISMS

The antibacterial activity of the green-synthesized rGO–Ag@PANI nanocomposite is primarily attributed to the generation of reactive oxygen species (ROS), hydroxyl radicals (•OH), hydrogen peroxide (H_2O_2), and singlet oxygen ($^1O_2$). These ROS are generated through synergistic interactions among the composite's components—silver nanoparticles (Ag NPs), reduced graphene oxide (rGO), and polyaniline (PANI). Ag NPs catalyze the formation of ROS under ambient conditions, while rGO enhances electron transport and serves as a conductive support figure 9. PANI contributes to redox cycling and further amplifies ROS production. Once introduced into a bacterial environment, the rGO–Ag@PANI nanocomposite adheres to the bacterial cell surface due to electrostatic interactions and high surface area, enabling direct contact and efficient ROS-mediated action. The generated ROS induce lipid peroxidation, leading to disruption of the bacterial membrane, while concurrently damaging intracellular proteins and causing DNA fragmentation. These oxidative stresses ultimately result in membrane leakage, enzyme inactivation, and bacterial cell death. The effects are particularly significant in Gram-negative bacteria such as *Escherichia coli* and *Pseudomonas aeruginosa*, where the relatively thinner peptidoglycan layer and higher membrane permeability facilitate rapid ROS penetration and damage. Experimental findings support this mechanism, as demonstrated by significantly lower MIC values (3.125 µg/mL for *E. coli* and 6.25 µg/mL for *Pseudomonas*), larger inhibition zones, and high bacteriostatic rates (95% and 92.5%, respectively) observed for the rGO–Ag@PANI composite compared to its individual components. These results collectively confirm that ROS generation plays a central role in the enhanced antibacterial efficacy of the rGO–Ag@PANI nanocomposite.

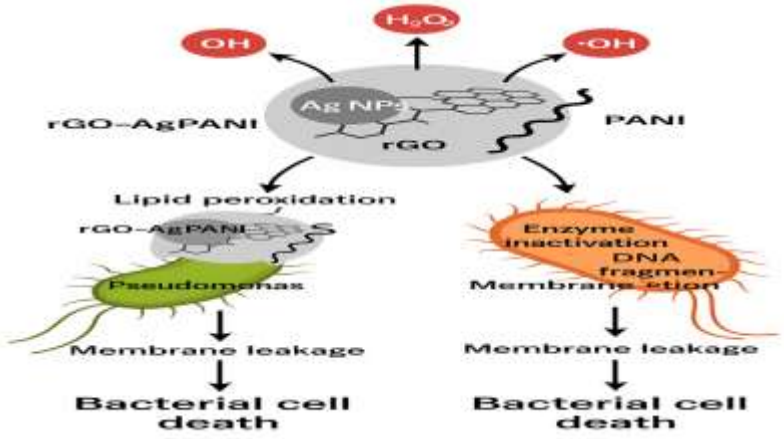

Figure 9. ROS mechanism against *Escherichia coli* and *Pseudomonas*

4. CONCLUSION

The antibacterial efficacy of synthesized materials—PANI, rGO, Ag nanoparticles, rGO–Ag nanocomposite, and the hybrid rGO–Ag/PANI composite—was systematically evaluated against two Gram-negative bacterial strains, *Escherichia coli* and *Pseudomonas aeruginosa*. The zone of inhibition test revealed a clear concentration-dependent antibacterial effect for both PANI and rGO–Ag/PANI nanocomposite. As the concentration increased from 100 to 300 µg/mL, the diameter of inhibition zones also expanded, indicating enhanced bacterial growth suppression. Specifically, PANI showed inhibition zones against *Pseudomonas* of 13.0 mm, 20.0 mm, and 22.5 mm, and against *E. coli* of 12.5 mm, 11.5 mm, and 14.5 mm for 100, 200, and 300 µg/mL concentrations respectively. Meanwhile, the rGO–Ag/PANI nanocomposite demonstrated significantly larger zones of inhibition across all concentrations, with maximum diameters reaching 27.0 mm against *Pseudomonas* and 23.0 mm against *E. coli* at 300 µg/mL. These results underscore the superior antibacterial performance of the composite material compared to PANI alone.

Complementary to these observations, Minimum Inhibitory Concentration (MIC) testing provided quantitative insight into the antimicrobial potency of all materials. MIC is defined as the lowest concentration at which a material inhibits visible bacterial growth in a liquid medium. Lower MIC values correspond to stronger antibacterial activity. Among the materials examined, rGO–Ag/PANI exhibited the lowest MIC values of 3.125 µg/mL for *E. coli* and 6.25 µg/mL for *Pseudomonas*, indicating its high efficacy at minimal concentrations. In contrast, rGO alone showed the weakest activity, with MIC values of 50 µg/mL and 100 µg/mL against *E. coli* and *Pseudomonas*, respectively. The superior antibacterial performance of the rGO–Ag/PANI composite can be attributed to a synergistic combination of its constituents. Silver nanoparticles contribute potent bactericidal action through the release of Ag^+ ions, which disrupt cellular processes. Reduced graphene oxide offers physical disruption of bacterial membranes and facilitates electron transfer, while polyaniline enhances surface interactions and electrical conductivity, potentially amplifying the antibacterial mechanisms.

In conclusion, the multi-component rGO–Ag/PANI nanocomposite exhibits markedly improved antibacterial activity against Gram-negative bacteria compared to its individual components, as evidenced by both increased zones of inhibition and significantly lower MIC values. This synergy among silver, graphene-based materials, and conducting polymers suggests that rGO–Ag/PANI is a promising candidate for antimicrobial applications, particularly in environments where strong bacterial resistance is a challenge. Future work should explore its efficacy against a broader spectrum of pathogens and evaluate its potential integration into water treatment systems and medical devices.

5. Interests In Conflict: There aren't any declared conflicts.

6. Availability Of Data Statement

The data supporting the findings of the research will be made available upon request by the corresponding author. Ethical and privacy concerns prevent the general public from accessing the figures.

7. Declarations

The authors' original data and results are included in the study, which was not submitted for publication anywhere else.

8. Contributions Of the Authors: To this manuscript, each author has contributed equally.

REFERENCE

1. Adimalla, N. and Qian, H., 2019. Groundwater quality evaluation using water quality index (WQI) for drinking purposes and human health risk (HHR) assessment in an agricultural region of Nanganur, south India. *Ecotoxicology and environmental safety*, *176*, pp.153-161.

2. Lin, L., Yang, H. and Xu, X., 2022. Effects of water pollution on human health and disease heterogeneity: a review. *Frontiers in environmental science*, *10*, p.880246.

3. Adimalla, N., Li, P. and Qian, H., 2019. Evaluation of groundwater contamination for fluoride and nitrate in semi-arid region of Nirmal Province, South India: a special emphasis on human health risk assessment (HHRA). *Human and ecological risk assessment: an international journal*.

4. Radfard, M., Yunesian, M., Nabizadeh, R., Biglari, H., Nazmara, S., Hadi, M., Yousefi, N., Yousefi, M., Abbasnia, A. and Mahvi, A.H., 2019. Drinking water quality and arsenic health risk assessment in Sistan and Baluchestan, Southeastern Province, Iran. *Human and ecological risk assessment: An International Journal*.
5. Chen, J., Wu, H., Qian, H. and Gao, Y., 2017. Assessing nitrate and fluoride contaminants in drinking water and their health risk of rural residents living in a semiarid region of Northwest China. *Exposure and Health*, *9*, pp.183-195.
6. Landrigan, P.J., Stegeman, J.J., Fleming, L.E., Allemand, D., Anderson, D.M., Backer, L.C., Brucker-Davis, F., Chevalier, N., Corra, L., Czerucka, D. and Bottein, M.Y.D., 2020. Human health and ocean pollution. *Annals of global health*, *86*(1).
7. Amarasiri, M., Sano, D. and Suzuki, S., 2020. Understanding human health risks caused by antibiotic resistant bacteria (ARB) and antibiotic resistance genes (ARG) in water environments: Current knowledge and questions to be answered. *Critical Reviews in Environmental Science and Technology*, *50*(19), pp.2016-2059.
8. Mohammadi, A.A., Zarei, A., Majidi, S., Ghaderpoury, A., Hashempour, Y., Saghi, M.H., Alinejad, A., Yousefi, M., Hosseingholizadeh, N. and Ghaderpoori, M., 2019. Carcinogenic and non-carcinogenic health risk assessment of heavy metals in drinking water of Khorramabad, Iran. *MethodsX*, *6*, pp.1642-1651.
9. Siddiqua, A., Hahladakis, J.N. and Al-Attiya, W.A.K., 2022. An overview of the environmental pollution and health effects associated with waste landfilling and open dumping. *Environmental Science and Pollution Research*, *29*(39), pp.58514-58536.
10. Juntunen, J., Meriläinen, P. and Simola, A., 2017. Public health and economic risk assessment of waterborne contaminants and pathogens in Finland. *Science of the Total Environment*, *599*, pp.873-882.
11. Greco, S.L., Drudge, C., Fernandes, R., Kim, J. and Copes, R., 2020. Estimates of healthcare utilisation and deaths from waterborne pathogen exposure in Ontario, Canada. *Epidemiology & Infection*, *148*, p.e70.
12. Collier, S.A., Deng, L., Adam, E.A., Benedict, K.M., Beshearse, E.M., Blackstock, A.J., Bruce, B.B., Derado, G., Edens, C., Fullerton, K.E. and Gargano, J.W., 2021. Estimate of burden and direct healthcare cost of infectious waterborne disease in the United States. *Emerging infectious diseases*, *27*(1), p.140.
13. Semenza, J.C. and Ko, A.I., 2023. Waterborne diseases that are sensitive to climate variability and climate change. *New England Journal of Medicine*, *389*(23), pp.2175-2187.
14. Chiang, C.C., Breslin, J., Weeks, S. and Meng, Z., 2021. Dynamic mechanical behaviors of nacre-inspired graphene-polymer nanocomposites depending on internal nanostructures. *Extreme Mechanics Letters*, *49*, p.101451.
15. del Bosque, A., Muñoz, B.K., Sánchez, M. and Ureña, A., 2022. Thermomechanically robust ceramic/polymer nanocomposites modified with ionic liquid for hybrid polymer electrolyte applications. *ACS Applied Energy Materials*, *5*(4), pp.4247-4258.
16. Loeb, S.K., Alvarez, P.J., Brame, J.A., Cates, E.L., Choi, W., Crittenden, J., Dionysiou, D.D., Li, Q., Li-Puma, G., Quan, X. and Sedlak, D.L., 2018. The technology horizon for photocatalytic water treatment: sunrise or sunset?
17. Chaudhary, R., Singh, N.B., Nagpal, G. and Saah, F.K., 2024. Antibacterial activity of reduced graphene-silver oxide nanocomposite against gram-negative bacteria. *The Microbe*, *5*, p.100221.
18. Deshmukh, M.A., Kang, B.C. and Ha, T.J., 2020. Non-enzymatic electrochemical glucose sensors based on polyaniline/reduced-graphene-oxide nanocomposites functionalized with silver nanoparticles. *Journal of Materials Chemistry C*, *8*(15), pp.5112-5123.
19. Weinstein, M.P. and Lewis, J.S., 2020. The clinical and laboratory standards institute subcommittee on antimicrobial susceptibility testing: background, organization, functions, and processes. *Journal of clinical microbiology*, *58*(3), pp.10-1128.
20. Gasaymeh, S.S. and ALmansoori, N.N., 2020. Novel formation mechanism of Ag/PANI/PVP core-shell nanocomposites. *Results in Physics*, *16*, p.102882.
21. Kaladevi, G., Wilson, P. and Pandian, K., 2020. Simultaneous and selective electrochemical detection of sulfite and nitrite in water sources using homogeneously dispersed Ag nanoparticles over PANI/rGO nanocomposite. *Journal of The Electrochemical Society*, *167*(2), p.027514.
22. Shubhadarshinee, L., Jali, B.R., Barick, A.K. and Mohapatra, P., 2022. Preparation and characterisation of silver nanoparticles/graphene oxide hybrid nanofiller reinforced-polyaniline. *Plastics, Rubber and Composites*, *51*(2), pp.72-84.
23. Maruthapandi, M., Saravanan, A., Gupta, A., Luong, J.H. and Gedanken, A., 2022. Antimicrobial activities of conducting polymers and their composites. Macromol, 2(1), pp.78-99.
24. Kowalska-Krochmal, B. and Dudek-Wicher, R., 2021. The minimum inhibitory concentration of antibiotics: methods, interpretation, clinical relevance. *Pathogens*, *10*(2), p.165.
25. Zhang, X., Wang, X., Cheng, H., Zheng, Y., Zhao, J. and Qu, K., 2021. A universal automated method for determining the bacteriostatic activity of nanomaterials. *Journal of Hazardous Materials*, *413*, p.125320.